Transport in Porous Media
https://doi.org/10.1007/s11242-024-02122-8

# A Pore-Level Study of Dense-Phase $CO_2$ Foam Stability in the Presence of Oil

**Benyamine Benali[1] · Martin A. Fernø[1,2] · Hilde Halsøy[1] · Zachary Paul Alcorn[1]**

Received: 12 February 2024 / Accepted: 14 August 2024


## Abstract

The ability of foam to reduce $CO_2$ mobility in $CO_2$ sequestration and $CO_2$ enhanced oil recovery processes relies on maintaining foam stability in the reservoir. Foams can destabilize in the presence of oil due to mechanisms impacting individual lamellae. Few attempts have been made to measure the stability of $CO_2$ foams in the presence of oil in a realistic pore network at reservoir pressure. Utilizing lab-on-a-chip technology, the pore-level stability of dense-phase $CO_2$ foam in the presence of a miscible and an immiscible oil was investigated. A secondary objective was to determine the impact of increasing surfactant concentration and nanoparticles on foam stability.

In the absence of oil, all surfactant-based foaming solutions generated fine-textured and strong foam that was less stable both when increasing surfactant concentrations and when adding nanoparticles. Ostwald ripening was the primary destabilization mechanism both in the absence of oil and in the presence of immiscible oil. Moreover, foam was less stable in the presence of miscible oil, compared to immiscible oil, where the primary destabilization mechanism was lamellae rupture. Overall, direct pore-scale observations of dense-phase $CO_2$ foam in realistic pore network revealed foam destabilization mechanisms at high-pressure conditions.

## Highlights

- **Pore-scale observations of dense-phase $CO_2$ foam in realistic pore network revealed foam destabilization mechanisms at high-pressure conditions.**
- **A comprehensive laboratory investigation of CO2 foam stability in the presence of oil at high pressure.**

**Keywords** $CO_2$ foam · $CO_2$ storage · $CO_2$ EOR · Foam stability · Oleic phase · $CO_2$ mobility control · Pore scale

✉ Benyamine Benali
benyamine.benali@uib.no

[1] Department of Physics and Technology, University of Bergen, Bergen, Norway

[2] NORCE Norwegian Research Centre AS, Nygårdsgaten 112, 5008 Bergen, Norway

## 1 Introduction

Climate change, driven by industrial human activity, has increased the frequency and intensity of extreme events resulting in significant damages to the environment and human communities, extending beyond what can be attributed to natural climate variability. There is a clear need to reduce greenhouse gas emissions associated with industrial human activity to mitigate the impacts of climate change. Geological $CO_2$ sequestration has emerged as a crucial part of the solution. The estimated technical geological $CO_2$ sequestration capacity exceeds 1000 $GtCO_2$, surpassing the necessary requirements for $CO_2$ sequestration to limit global warming to 1.5 °C by the year 2100 (Lee et al. 2023). Therefore, carbon capture, utilization and sequestration (CCUS) is essential to mitigate climate change. CCUS encompasses the capture of $CO_2$ from industrial sources, including cement or power plants. The captured $CO_2$ is then injected into subsurface reservoirs for geological carbon sequestration (Metz et al. 2005). The captured $CO_2$ can also be injected into depleted oil and gas fields and utilized in enhanced oil recovery (EOR) processes (Hannis et al. 2017).

Over the past decades, $CO_2$ injection for EOR and carbon sequestration has been widely implemented (Taber et al. 1997; Eiken et al. 2011). Despite successful applications of $CO_2$ EOR and sequestration, their effectiveness is hampered by challenges related to high $CO_2$ mobility and reservoir heterogeneity (Hanssen et al. 1994). The lower viscosity and density of $CO_2$ compared to other reservoir fluids can lead to viscous fingering and gravity override, whereas reservoir heterogeneity may result in channeling through highly permeable zones (Mo et al. 2012; Talebian et al. 2014; Alcorn et al. 2020a). These challenges contribute to poor sweep efficiency, elevated gas-oil ratios, diminished oil recovery, and a reduced capacity for $CO_2$ sequestration (Lake et al.). $CO_2$ foam has emerged as a solution for mitigating these flow instabilities by increasing $CO_2$ viscosity, reducing its relative permeability, and diverting flow from high- to lower-permeability zones (Rossen 1996; Enick et al. 2012; Føyen et al. 2020; Sæle et al. 2022).

$CO_2$ foam consists of a discontinuous phase ($CO_2$) dispersed in a continuous liquid phase (David & Marsden 1969). Foam is generated in porous media by injecting a solution containing surfactants and/or nanoparticles and $CO_2$ (Shan & Rossen 2004). Maintaining foam stability is critical to the success of foam applications. Foam stability refers to the time over which foam maintains its initially generated properties (Roy Choudhury 2013). Foam stability is notably influenced by the surfactant concentration, particularly in the proximity of the critical micelle concentration (CMC). However, this relationship weakens considerably when concentrations increase beyond the CMC, where more thermodynamically stable micelles are formed (Wang et al. 2017). Maintaining foam stability, especially in harsh reservoir conditions, is challenging for surfactant-based foams due to surfactant adsorption on rock material and the presence of oil (Sheng 2013). Nanoparticles have been shown to enhance foam stability under harsh reservoir conditions (Eide et al. 2018). However, when used alone, they result in weaker foam compared to surfactants (Alcorn et al. 2020b; Soyke et al. 2021). This enhancement is attributed to the trapping of nanoparticles in lamellae (liquid film separating $CO_2$ bubbles) and plateau borders (the position where three lamellae meet), hindering coalescence and liquid drainage (Singh & Mohanty 2014). Foam stability depends on the longevity of individual lamellae (Farajzadeh et al. 2012), which undergo movement and rearrangement after bubble generation to achieve minimum interfacial free energy (Aronson et al. 1994). This leads to changes in foam texture influencing bubble size and number, driven by three mechanisms: drainage, where lamellae thin due to gravity or capillary suction (Kovscek & Radke 1993), coalescence, where bubbles merge and create larger bubbles as a result of

lamella rupture (Langevin 2019), and coarsening, where gas diffuses through lamellae as a result of variations in capillary pressure, also known as Ostwald ripening (Voorhees 1985, 1992; Benali et al. 2023).

At the pore scale, the influence of surface forces surpasses volumetric forces, rendering the drainage mechanism negligible (Yu & Kanj 2022). Bubble coalescence is notably diminished and can be disregarded in surfactant-based foams, where surfactants enhance lamella's interfacial properties and restrict bubble rupture (Huang et al. 2017; Yu et al. 2022). Consequently, Ostwald ripening emerges as the dominant coarsening mechanism governing foam stability at the pore scale. Foam coarsening during $CO_2$ EOR is unfavorable because it leads to an increase in foam mobility, resulting in decreased sweep efficiency, whereas it can be favorable during $CO_2$ sequestration because it leads to stable $CO_2$ bubbles trapped in the pores. Ostwald ripening is a well-known phenomenon in bulk systems (Greenwood 1956; Lifshitz & Slyozov 1961; Voorhees 1985, 1992; Benali et al. 2023). It entails the movement of gas from smaller bubbles possessing a small radius, high curvature, and high internal pressure to larger bubbles with a large radius, low curvature, and low internal pressure. This process leads to the disappearance of smaller bubbles (Saint-Jalmes 2006; Marchalot et al. 2008). However, the process becomes more complex in porous media because the bubbles encounter constraints on free growth and the coarsening is influenced by the geometric confinement of the pores (Xu et al. 2019; Yu & Kanj 2022).

In depleted oil fields, foam encounters oil in the reservoir which influences its stability. The oil exists in either a miscible or immiscible state with $CO_2$, each exerting distinct effects on the $CO_2$ foam. In the case of miscible oil, $CO_2$ and oil coexist in a single phase with varying $CO_2$ concentrations in the oil, resulting in a system primarily composed of an aqueous phase and a mixture of $CO_2$ and oil. For the immiscible oil, three phases will coexist. The miscible oil alters the interfacial properties of the foam, thereby impacting the stability of lamellae. On the other hand, for immiscible oil, four primary theories explore the impact of oil on foam stability: (1) entering and spreading (Bergeron et al. 1993), (2) lamella number (Schramm & Novosad 1990), (3) bridging (Garrett 1980), and (4) pseudo-emulsion film theory (Raterman 1989).

Few attempts have been made to understand the stability of dense-phase $CO_2$ foams in the presence of oil in a realistic pore network at reservoir pressure. However, it is critical to gain an in-depth understanding of $CO_2$ foam stability at reservoir pressure because interfacial tension decreases and $CO_2$ viscosity and density increases, compared to standard pressure conditions. Furthermore, the $CO_2$ foam stability is influenced by $CO_2$ miscibility with oil. Therefore, the main objective of this work was to study the pore-level stability of dense-phase $CO_2$ foam, generated with different foaming solutions, in the presence of miscible and immiscible oil at 100 bars and 23 °C. A secondary objective was to determine the impact of increasing surfactant concentration and including nanoparticles on foam stability, in the absence and presence of oil. High-pressure micromodels offered a direct visualization method for observing $CO_2$ foam and oil interactions in porous media. These two-dimensional flow cells feature a pore network and transparent glass for visualization [41]. The foam bubbles were monitored using high-resolution images acquired by a Zeiss microscope. Image analysis techniques were employed to monitor changes in bubble number (Rognmo et al. 2019; Gizzatov et al. 2021).

## 2 Materials and Methods

### 2.1 Fluid Preparation

Brine (35,000 ppm NaCl) containing fluorescein sodium salt (500 ppm $C_{20}H_{10}Na_2O_5$, F6377 Sigma-Aldrich) was used for all aqueous phases (Table 1). Neuro-dil fluorescence ($2.9 \times 10^{-5} M$, #60,016-Biotium BioNordika) was added to the solutions to optically distinguish between the aqueous, oleic and gaseous phases. Prior to injection into the micromodel, all the solutions were filtered using a sterile 0.2 µm cellulose acetate filter (514–0061, VWR). Two foaming agents were utilized: (1) Surfonic L24-22 (Indorama Ventures) is a non-ionic, water-soluble surfactant with linear ethoxylated alcohol and a CMC of 100 ppm, and (2) Levasil CC301 (Nouryon) is a surface-modified spherical silica nanoparticle. The miscible oil was n-decane ($C_{10}H_{22}$) with a minimum miscibility pressure (MMP) to $CO_2$ of 56 bar at 22 °C (Pereponov et al. 2023), whereas the immiscible oil was a North Sea crude oil from a chalk reservoir with a MMP of 125 bar at 75 °C (Steinsbø et al. 2014) and API of 33.6 ° (Alcorn et al. 2020a). $CO_2$ of 99.999% purity was used for foam generation and to saturate the aqueous solution before injecting it into the micromodel. Four foaming solutions were prepared by mixing brine with surfactant, nanoparticle, or a hybrid combination of both (Table 1).

### 2.2 Micromodel

A custom-designed, high-pressure micromodel facilitated the direct observation of pore-scale interactions among various fluids and rock grains under reservoir conditions (Benali 2019; Alcorn et al. 2020b; Benali et al. 2022; Benali et al. 2023; Liu et al. 2023). With an optically transparent borosilicate glass bonded to a silicon wafer etched with a representative pore structure, this 2D model was developed from thin sections of a natural sandstone. The silicon wafer micromodel, created using deep reactive ion etching, featured a constant depth of 30 µm to ensure vertical pore walls and sharp edges. To convert 3D porous matrix from a rock sample to 2D, some adjustments were made to interconnect all pores, resulting in elevated porosity and permeability compared to cylindrical sandstone samples (Buchgraber et al. 2012). The distinct pore network ($7.2 \times 2.8$ mm) was replicated 36 times ($4 \times 9$) with an overlap, creating a comprehensive

**Table 1** Composition of solutions

| Aqueous solution | Concentration, component |
|---|---|
| Brine | 35 000 ppm, NaCl |
| Aqueous fluorescent dye | 500 ppm, fluorescein sodium salt |
| Oil fluorescent dye | 31 ppm, neuro dil |
| Surfactant (SF) 5000 | 5000 ppm, Surfonic L24-22 |
| Surfactant (SF) 2500 | 2500 ppm, Surfonic L24-22 |
| Surfactant (SF) 2500 + Nanoparticle (NP) 1500 | 2500 ppm, Surfonic L24-22 + 1500 ppm, Levasil CC301 |
| Nanoparticle (NP) 1500 | 1500 ppm, Levasil CC301 |
| IPA | 877 000 ppm, 2-propanol-water azeotrope |
| Hydrogen peroxide | 300 000 ppm, $H_2O_2$ |

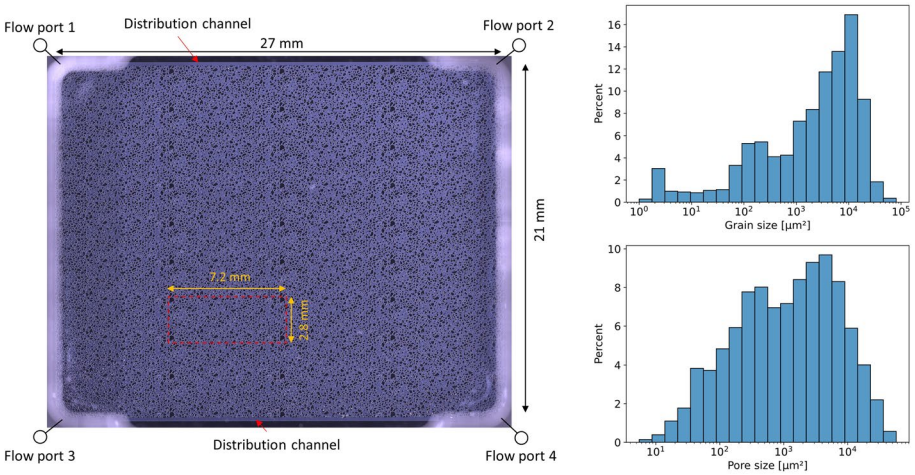


**Fig. 1** Left: The overall dimensions of the micromodel, including the distinctive pore network, fluid flow ports, and distribution channels. Right: characteristic attributes of the micromodel from one of the 36 repetitions are shown. The top graph displays grain sizes, whereas the bottom graph illustrates the distribution of pore sizes. The average grain and pore sizes are 6238 µm$^2$ and 3896 µm$^2$, respectively

pore network spanning 27 × 21 mm (Fig. 1). Additionally, the micromodel featured two fluid distribution channels (200 µm width), positioned at the top and bottom. Four flow ports were etched through the silicon wafer, establishing connections with external environments. Key micromodel properties are presented in Table 2. Porosity and permeability were calculated to be 0.61 and 2.97 Darcy, respectively (Benali 2019). The pore volume (PV) was 11.1 µL (Benali 2019). Employing the snow algorithm for pore classification (Gostick et al. 2019), the average pore size was determined to be 3896 µm$^2$.

**Table 2** Pore network properties

| Parameter | Value |
|---|---|
| Width | 27 mm |
| Length (without channels) | 21 mm |
| Depth | 30 µm |
| Porosity | 0.61 |
| Permeability | 2.97 Darcy |
| Average pore size | 3896 µm$^2$ |
| Unique pore network repetition | 36 |
| Pattern size | 7.2 mm × 2.8 mm |
| Tortuosity ($x$-axis) | 1.881 |
| Tortuosity ($y$-axis) | 1.998 |
| Wettability | Water-wet |

### 2.3 Experimental Setup and Procedures

Images of the pore network were acquired using a microscope (Axio Zoom. V16, Zeiss) equipped with both brightfield and fluorescence channels. The brightfield channel used a cold-light source and a diffuser S for uniform illumination. The fluorescence channel used to track the aqueous phase was a 38 HE Green fluorescent reflector, and to track the oil phase a 43 HE DsRed fluorescent reflector was used. A motorized scanning stage enabled high-resolution image acquisition by using 121 tiles (11 × 11). Three images were captured for each tile and then stitched together within a time frame of 9 min to obtain images of the whole pore network at three channels (two fluorescence channel images and one brightfield channel image). Detailed description of image analysis steps can be found elsewhere (Benali et al. 2023).

The number of bubbles (NB) was used to describe the texture of the foam and to quantify the normalized bubble number ($N_{\mathrm{NB}}$) as a function of time to study the stability of the surfactant-based foam systems. The $N_{\mathrm{NB}}$ was defined as:

$$N_{\mathrm{NB}} = \frac{\mathrm{NB}}{\mathrm{NB}_i} \tag{1}$$

where $\mathrm{NB}_i$ is the initial bubble number.

The rate of change in $N_{\mathrm{NB}}$ ($\mathrm{d}N_{\mathrm{NB}}/\mathrm{dt}$) was utilized to evaluate the foam total stability time (ST):

$$ST = \sum \left| \frac{dN_{NB}}{dt} \right| < 0.002 \tag{2}$$

The specified range of 0.002 in the rate of change of the $N_{\mathrm{NB}}$ was selected to capture a threshold where the foam undergoes minimal, yet detectable, changes. This range was deemed appropriate for identifying a stable foam state because it represents a balance between sensitivity to changes in bubble number and robustness against minor fluctuations. Additionally, the selected observation period of 10% of the experimental time, equivalent to 298 min, ensures a comprehensive assessment of foam behavior providing a reliable basis for stability determination.

Figure 2 shows a schematic of the high-pressure experimental setup. A back pressure regulator (BPR) connected to a $N_2$ cylinder was used to hold the experimental pressure at 100 bar. The select valves allowed injection and production from all the flow ports. The switch valve was used to inject incompressible fluids directly into the micromodel using the pump with distilled water as driving force. The cleaning solutions were injected into the 1 mL filling loop in the switch valve using a syringe, then the switch valve passed through the loop, and the solutions were pressurized the same as the system (Fig. 2). Prior to injection into the pore network, all aqueous solutions were saturated with liquid $CO_2$ at experimental conditions, enabling the intensity of the fluorescence dye to stay constant when contacting $CO_2$. Before each experiment the pore network was cleaned with distilled water, 2-propanol-water azeotrope (IPA), and hydrogen peroxide ($H_2O_2$). $H_2O_2$ was used to maintain the same surface conditions before each experiment. The $CO_2$ was in the liquid phase at experimental conditions of 100 bar and 23 °C (Eric W. Lemmon et al. 2023).

Investigation of the Ostwald ripening mechanism and the effect of oil for a static $CO_2$ foam in porous media at high pressure requires stable $CO_2$ saturation in the field of view (FoV). The experiments were designed to keep the $CO_2$ saturation constant throughout the experiment. Consistent pore geometry is maintained throughout this study to isolate

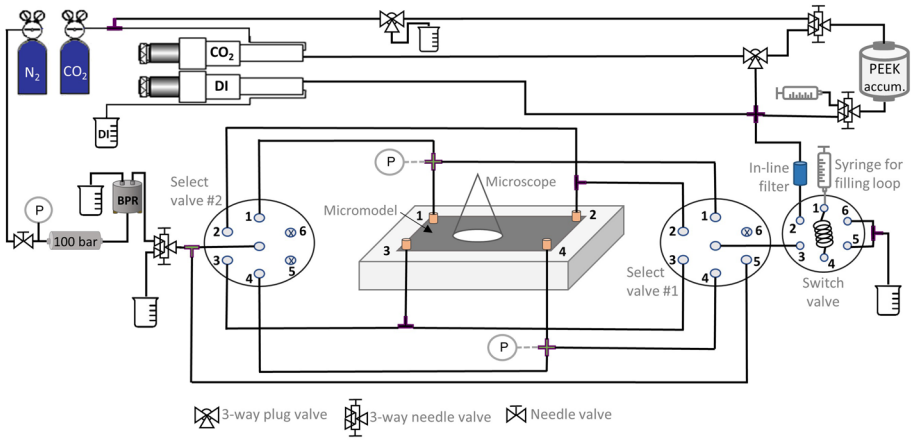


**Fig. 2** Schematic of the experimental setup used for pore-scale foam investigations in the micromodel. The micromodel was set up in the holder positioned beneath the microscope. Although the lines were connected to the ports from the bottom side of the holder, they are drawn at the top in the figure for clarity. Fluid injection was carried out using a high-precision plunger pump (Quizix Q5000− 2.5 K). The DI cylinder was employed for injecting distilled water or propelling fluids in the loop in the switch valve, while the $CO_2$ cylinder was utilized for $CO_2$ injection or propelling fluids from the PEEK accumulator. To maintain a constant dead volume, two 6-port select valves (Idex, MXP7970-000) were placed, one at the inlet (#1) and one at the outlet (#2). Additionally, a two-position switch valve (Idex, 9725) was integrated to facilitate variable fluid injection without the need for extra pumps (Benali et al. 2023)

its influence. Experiment without oil present was conducted to benchmark the subsequent foam stability tests in the presence of oil.

The following procedure was used in the absence of oil:

i. Inject the $CO_2$-saturated foaming solutions at a constant volumetric flow rate (2 µL/min) using port 1 for injection and port 4 for production, until fully saturated.
ii. Inject dense-phase $CO_2$ at a constant volumetric flow rate (2 µL/min)for 2 h to generate foam with high $CO_2$ saturation and bubble number, using port 1 for injection and port 4 for production.
iii. Inject the $CO_2$-saturated foaming solutions at a constant volumetric flow rate (1 µL/min) to remove the $CO_2$ bubbles in the distribution channels and isolate foam in the pore network, from port 1 to port 2, and port 3 to port 4 for 1 h each (5.4PV each).
iv. Hold constant pressure in the micromodel, using the distilled water cylinder, through port 1, while the production line was closed. $T=0$ min in the results and discussion section refers to this step, when the pump is connected to the micromodel.

The following procedure was used in the presence of oil:

i. Saturate the micromodel with distilled water at a constant volumetric flow rate (10 µL/min) using port 1 for injection and port 4 for production.
ii. Inject oil at a constant volumetric flow rate (10 µL/min) using port 1 for injection and port 4 for production.

iii. Inject the $CO_2$-saturated foaming solutions at a constant volumetric flow rate (2 µL/min) using port 1 for injection and port 4 for production, until the oil saturation was constant.
iv. Inject dense-phase $CO_2$ at a constant volumetric flow rate (2 µL/min) for 2 h, to generate foam with high $CO_2$ saturation and bubble number, using port 1 for injection and port 4 for production.
v. Inject the $CO_2$-saturated foaming solutions at a constant volumetric flow rate (1 µL/min) to remove the $CO_2$ bubbles in the distribution channels and isolate foam in the pore network, from port 1 to port 2, and port 3 to port 4 for 1 h each (5.4 PV each).
vi. Hold constant pressure in the micromodel, with the $CO_2$ pump, through the peek accumulator filled with the $CO_2$-saturated solution, using port 1 for injection while the production line was closed. $T=0$ min in the results and discussion section refers to this step, when the pump is connected to the micromodel.

## 3 Results

### 3.1 Foam Stability in the Absence of Oil

Figure 3 shows sequential pore-scale images of $CO_2$ foam stabilized with different foaming solutions in the absence of oil. Foaming solutions consisted of 2500 ppm surfactant (2500SF), 5000 ppm surfactant (5000SF), 2500 ppm surfactant and 1500 ppm nanoparticles (2500SF + 1500NP), and 1500 ppm nanoparticles (1500NP). The initial number of bubbles (cf. Figure 3, $T=0$ min) in the field of view (FoV) were: 57 (2500SF); 65 (5000SF); 76 (2500SF + 1500NP); 31 (1500NP); 6 (Brine). Hence, all surfactant-based solutions generated fine-textured (strong) foam compared to brine and pure nanoparticle solution. The frequency of coarsening events, resulting in the disappearance of bubbles, increased both when increasing the surfactant concentration and when adding nanoparticles to the surfactant solution (compare number of red arrows, Fig. 3). The increase in coarsening events was attributed to the higher bubble number; coarsening events increase with bubble number contributing to the foam reaching an equilibrium state where, on average, each bubble occupies a single pore. Brine and 1500 ppm nanoparticle solutions generated weak foams, where high stability was expected because the systems were in near-equilibrium state.

The $N_{NB}$ (see Eq. 1) as a function of time was used to study the stability of the surfactant-based systems (Fig. 4), and the rate of change in the $N_{NB}$ was used to determine the stability time, as described in Sect. 5. The final $N_{NB}$ (after 2980 min) was lower than the initial value ($N_{NB}=1.0$) for all foaming solutions: 0.91 for 2500SF; 0.71 for 5000SF; 0.72 for 2500SF + 1500NP. The criterion for foam stability (see Eq. 2) was first achieved (cf. inset) by the 2500SF solution (after 260 min, blue up-faced triangle), followed by the 2500SF + 1500NP solution (after 460 min, green up-faced triangle), and finally, the 5000SF solution (1280 min, orange up-faced triangle). When stability was achieved, each foaming solution remained stable (i.e., curves contained with the stability region, cf. Figure 4, inset plot, blue shaded area) with minimal fluctuations. The decrease in stability time resulted from the increased bubble number, as more coarsening was expected for higher bubble number.

The 2500SF + 1500NP solution (highest initial bubble number: 76) exhibited the highest mean coarsening rate between $T=0$ min and the time when the curves first enter the

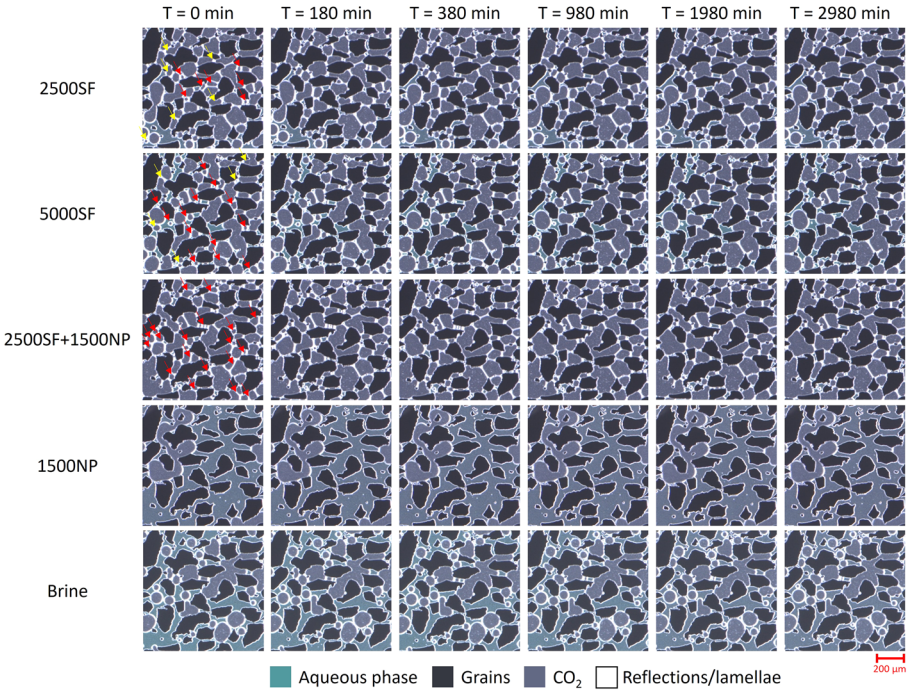


**Fig. 3** Sequential composed pore-scale images of the same field of view (0.87 mm × 0.87 mm) showing static $CO_2$ foam for five experiments: 2500 ppm surfactant (2500SF), 5000 ppm surfactant (5000SF), 2500 ppm surfactant and 1500 ppm nanoparticles (2500SF + 1500NP), 1500 ppm nanoparticles (1500NP), and Brine. The initial bubble number was 57, 65, 76, 6, and 31 for all the solutions from top to bottom. The red arrows indicate coarsening between $T=0$ and $T=2980$ min, where the number of bubbles was reduced, whereas the yellow arrows indicate coarsening where the number of bubbles remained unchanged. The hybrid solution containing nanoparticles (2500SF + 1500NP) had the largest reduction in the number of bubbles, whereas 2500SF had the smallest reduction in the number of bubbles

stability region: −0.004 for 2500SF; −0.006 for 5000SF; −0.011 for 2500SF + 1500NP (Fig. 4, inset plot). The mean coarsening time upon first entering the stability region increased for higher initial bubble number. Bubbles coarsen to reach a minimum energy state where, on average, each bubble occupies one pore (Xu et al. 2017; Jones et al. 2018). The 2500SF + 1500NP solution achieved stability more rapidly (after 460 min) compared with the 5000SF solution (after 1280 min), despite having a higher initial bubble number (76 vs 65). This observation can be attributed to the stabilizing effect of nanoparticles. As the number of lamellae decreased, the concentration of nanoparticles at new lamellae increased, effectively stabilizing the foam. Other experiments show that increasing the nanoparticle concentration leads to a decrease in interfacial tension, stabilizing the foam (Sarikhani et al. 2015).

### 3.2 Foam Stability in the Presence of Miscible Oil

Figure 5 shows sequential pore-scale images of $CO_2$ foam stabilized by different foaming solutions in the presence of miscible oil (*n*-decane). All surfactant-based solutions generated a finer-textured foam and higher initial number of bubbles (see Fig. 5,

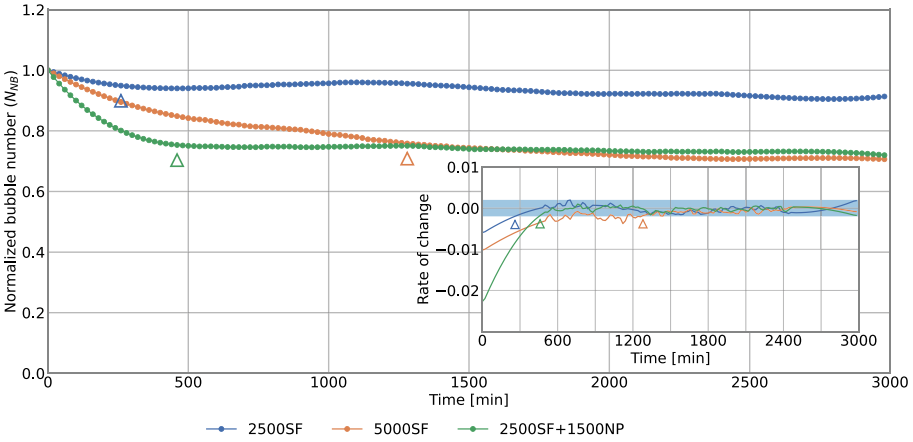


**Fig. 4** The normalized bubble number ($N_{NB}$) for experiments conducted with surfactant and nanoparticles-based solutions (2500SF, 5000SF, and 2500SF + 1500NP) versus time. The inset plot shows the rates of change in the $N_{NB}$. The blue shaded area shows the stability range. The triangles show the start of the stable state for the corresponding solution. The foams were stable starting from $T = 260$ min, $T = 1280$ min, and $T = 460$ min for 2500SF, 5000SF, and 2500SF + 1500NP, respectively. The stability was achieved first by the 2500SF solution at $T = 260$ min, followed by the hybrid solution at $T = 460$ min, and lastly, the 5000SF solution at $T = 1280$ min. Minimal changes in the rate of change occurred once the foam generated by the solutions entered the stability area

$T = 0$ min) compared to experiments without oil (expressed in parentheses): 2500SF: 104 (57); 5000SF: 80 (65); 2500SF + 1500NP: 97 (76); 1500NP: 9 (31); Brine: 12 (6). Doubling the surfactant concentration or adding nanoparticles decreased the number of initial bubbles, opposite of experiments in the absence of oil. Others have shown that the mean bubble diameter increases after reaching a minimum, because more thermodynamically stable micelles are generated (Wang et al. 2017), where increased mean bubble diameter translates to coarser foam. Fewer bubbles when increasing the surfactant concentration, or adding nanoparticles, indicated that the thermodynamically stable micelles/structures were generated at lower surfactant/nanoparticles concentrations when n-decane was present.

Foam coalescence, coarsening and regeneration events occurred in the presence of *n*-decane. Coarsening and coalescence areas are indicated by red arrows, whereas yellow polygons represent collapse of large bubbles leading to the generation of new bubbles (Fig. 5). Doubling the surfactant concentration resulted in fewer coarsening events, whereas the addition of nanoparticles to the surfactant solution led to more frequent coarsening events (compare the number of red arrows, Fig. 5). The 5000SF experienced fewer coarsening events compared to the 2500SF because it initially generated fewer bubbles. On the other hand, the 2500SF + 1500NP exhibited more coarsening events compared to the 2500SF, despite generating fewer bubbles. This suggests that the nanoparticles contributed to the generation of stable structures between nanoparticles and surfactants rather than solely stabilizing the lamellae. Brine and 1500 ppm nanoparticle generated a coarse-textured foam in the presence of *n*-decane, comparable to when oil was absent from the system. However, coarsening events (red and green polygons, 1500NP and Brine, Fig. 5) indicated a reduction in interfacial tension between *n*-decane/$CO_2$ and the aqueous phase. Figure 6 shows an example of the coalescence mechanism that occurred in many locations when *n*-decane was present.

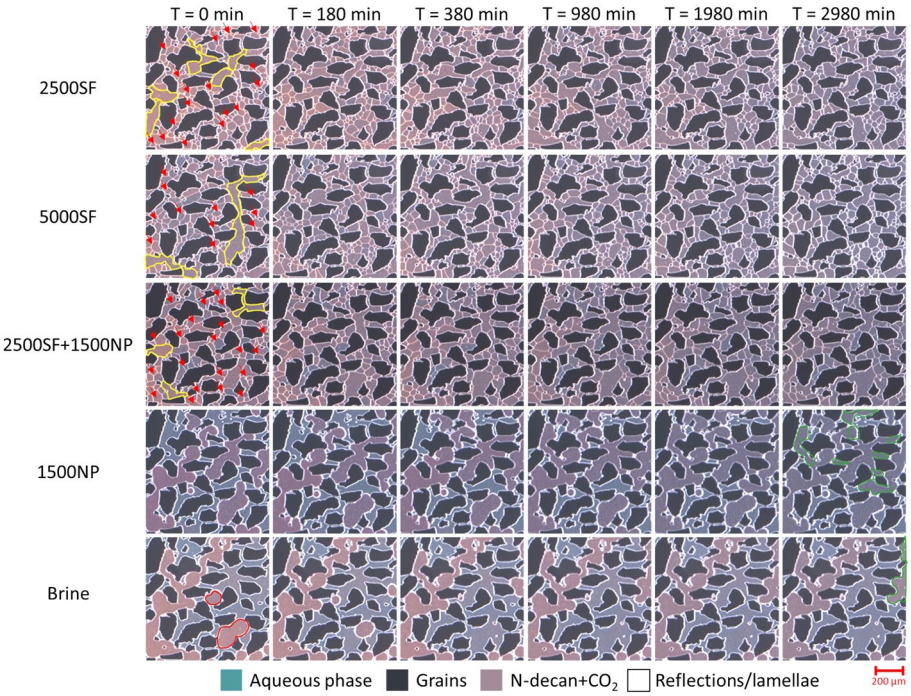


**Fig. 5** Sequential composed images at the same FoV (0.87 mm × 0.87 mm) show static $CO_2$ foam for five experiments conducted with different aqueous solutions (2500SF, 5000SF, 2500SF + 1500NP, 1500NP, and Brine) in the presence of n-decane. The bubble number at $T = 0$ min for all the solutions in the order presented in the figure were 104, 80, 97, 12, and 9. The red arrows indicate the locations where bubbles decayed. The yellow polygons indicate the large bubbles were bubble generation occurred. The red polygons show the bubble shrinkage due to the diffusion to larger bubbles shown as green polygons. The change in the red color with time is due to photobleaching. The hybrid solution containing nanoparticles (2500SF + 1500NP) had the most coarsening events, whereas the 5000SF had the least coarsening events

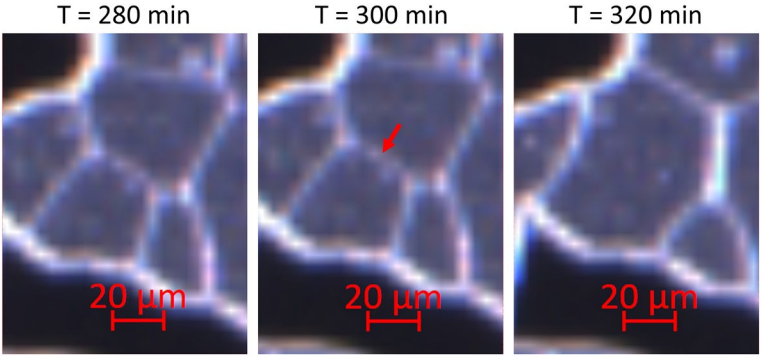


**Fig. 6** Sequential pore-scale images at the same FoV showing an example of coalescence occurrence for the 2500SF + 1500NP solution in the presence of *n*-decane. Grains appear black, *n*-decane and $CO_2$ appear purple, and grain edges and lamellae appear white. At $T = 300$ min, the red arrow shows a lamella that ruptured and disappeared at $T = 320$ min

The $N_{NB}$ was used to study the stability of the surfactant-based systems in the presence of n-decane (Fig. 7). The inset plot in Fig. 7 shows the rate of change in the $N_{NB}$ for all surfactant-based solutions. The 2500SF solution's $N_{NB}$ decreased to 0.86 after 2980 min (Fig. 7, blue curve) and held stability for 380 min starting from $T=200$ min (Fig. 7, inset plot, blue curve, and blue up-faced triangle). The 5000SF solution's $N_{NB}$ increased to 1.16 after 2980 min (Fig. 7, orange curve) and held stability for 440 min starting from $T=1680$ min (Fig. 7, inset plot, orange curve and orange up-faced triangle). The 2500SF + 1500NP solution's $N_{NB}$ decreased to 0.44 after 2980 min (Fig. 7, green curve) and never reached stability (Fig. 7, inset plot, green curve). The 5000SF held stability longer than the other foams, whereas the hybrid solution never reached stability. The foams that entered the stability region did not maintain stability for the entire experimental duration. Instead, foam coalescence and subsequent regeneration caused the foams to exit the stability region (Fig. 7, inset plot, down-faced triangles).

The foam texture was finer with decreased stability when n-decane was present compared to foam without oil where foam coarsening occurred due to $CO_2$ diffusion from small to larger bubbles. The primary foam destabilization mechanism in the presence of n-decane was lamellae rupture (coalescence). Doubling the surfactant concentration from 2500 to 5000 ppm increased foam stability, contrary to experiments without oil. In the presence of n-decane, a coarser foam was generated with the 5000SF solution compared to the 2500SF, and less coarsening was required to reach an equilibrium state. The hybrid solution (2500SF + 1500NP) generated less stable foam and lost more than 50% of the initial bubbles when *n*-decane was present, compared to 28% in the absence of oil. Therefore, adding nanoparticles to the solution resulted in the generation of more thermodynamically stable structures with less activity at the interface and foam destabilization through coalescence.

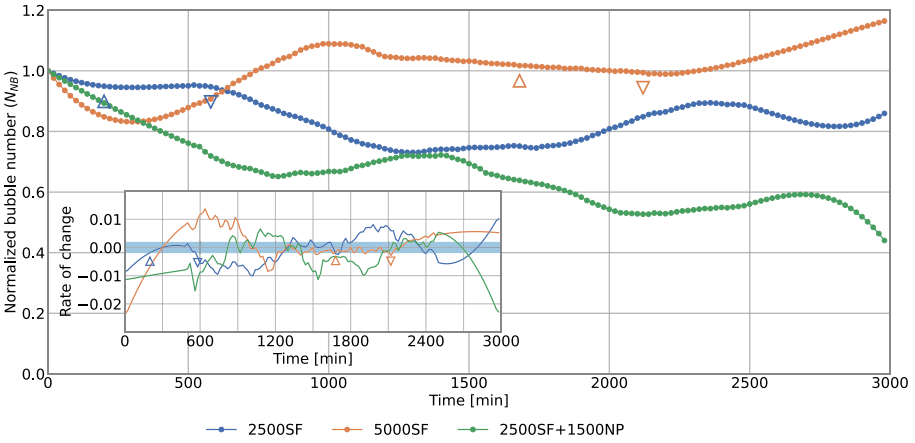


**Fig. 7** The normalized bubble number for experiments conducted with surfactant and nanoparticles-based solutions (2500SF, 5000SF, and 2500SF + 1500NP) in the presence of n-decane. The data points were smoothed using Savitzky–Golay filter. The inset plot shows the rates of change in the $N_{NB}$. The blue shaded area shows the stability range. The up-faced triangles show the start of the stability, whereas the down-faced triangles show the end of the stability for the different solutions. The foams were in stability in the time intervals: from $T=200$ min to $T=580$ min, and from $T=1680$ min to $T=2120$ min for 2500SF, and 5000SF, respectively. The initial bubble number was 104, 80, and 97 for all the solutions in the order presented in the figure. The hybrid solution (2500SF + 1500NP) generated less stable foam and lost more than 50% of the initial bubbles and did not held stability at all. Doubling the surfactant concentration from 2500 to 5000 ppm increased foam stability

### 3.3 Foam Stability in the Presence of Immiscible Oil

Figure 8 shows sequential pore-scale images of $CO_2$ foam stabilized by the various foaming solutions with crude oil present. The initial number of bubbles for the surfactant-based solutions was 131, 34, and 134 for 2500SF, 5000SF, and 2500SF + 1500NP, respectively (Fig. 8, $T = 0$ min). Adding the crude oil to the system resulted in generation of finer-textured foam compared to the presence of *n*-decane and the absence of oil. Doubling the surfactant concentration with the crude oil presence led to generation of a coarser-textured foam, as for the presence of n-decane. As for adding *n*-decane, adding crude oil also led to surpassing the minimum in the mean bubble diameter and generating coarser-textured foam when the surfactant concentration increased. Adding nanoparticles to the surfactant solution did not have an impact on the foam texture, as the initial bubble number was not significantly changed. Similar to the absence of oil and the presence of *n*-decane, in the presence of the crude oil, all surfactant-based solutions also generated fine-textured foam compared to the 1500NP solution, which generated 13 bubbles (Fig. 8, $T = 0$ min). The standalone use of nanoparticles was anticipated to produce a coarse-textured (weak) foam, as reported in several studies (Alcorn et al. 2020b; Soyke et al. 2021).

The frequency of coarsening events, resulting in the disappearance of bubbles, decreased when increasing the surfactant concentration and increased when adding nanoparticles to

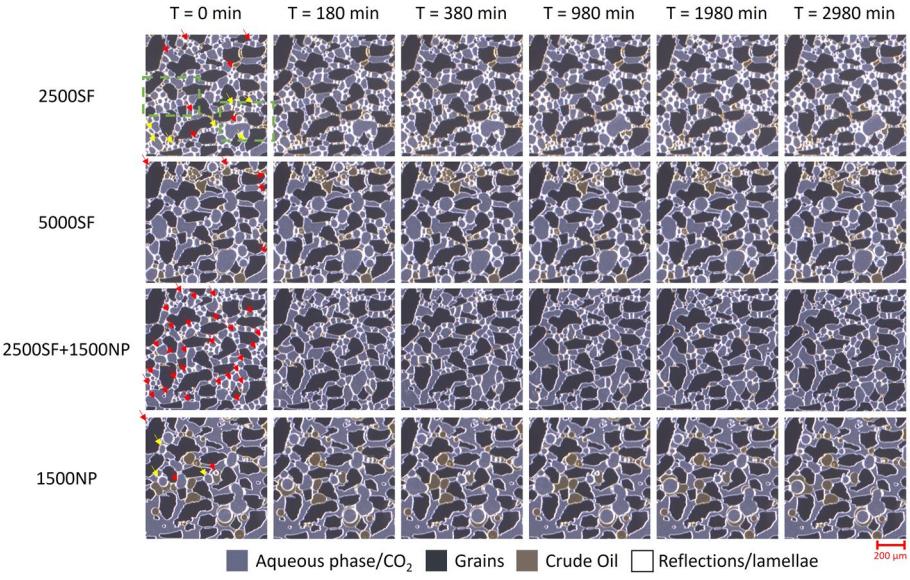


**Fig. 8** Sequential composed images at the same FoV (0.87 mm × 0.87 mm) showing static $CO_2$ foam for five experiments conducted with different aqueous solutions (2500SF, 5000SF, 2500SF + 1500NP, and 1500NP) in the presence of the crude oil. The bubble number at $T = 0$ min for all the solutions top to bottom was 131, 34, 134, and 13. The red arrows indicate coarsening where the number of bubbles was changed, whereas the yellow arrow indicates the coarsening where the number of bubbles remained unchanged. The green rectangles show the position of the two locations that were analyzed in the next section. Doubling the surfactant concentration led to a reduction in the coarsening events, as the 5000SF generated few bubbles, and the system was expected to be in near-equilibrium state. Adding nanoparticles led to an increase in the coarsening events although the initial number of bubbles was not significantly changed for the 2500SF and the 2500SF + 1500NP

the surfactant solution (compare the red arrows, Fig. 8). The decrease in coarsening events for the 5000SF compared to the 2500SF can be attributed to the low bubble number. The 5000SF was expected to be in a near-equilibrium state due to its low bubble number. As for the absence of oil, when the crude oil was present, adding nanoparticles led also to an increase in the coarsening events, although the initial number of bubbles was not significantly changed for the 2500SF and the 2500SF + 1500NP. The crude oil affected the 1500NP solution number of bubbles, where coarsening occurred (red arrows, 1500NP, Fig. 8) compared to the absence of oil with no coarsening.

The $N_{NB}$ was used to study the stability of the surfactant-based systems in the presence of crude oil (Fig. 9). The inset plot in Fig. 9 shows the rate of change in the $N_{NB}$ for all surfactant-based solutions. The 2500SF solution's $N_{NB}$ decreased to 0.95 after 2980 min (Fig. 9, blue curve) and held stability for 2820 min starting from $T = 160$ min (Fig. 9, inset plot, blue curve and blue up-faced triangle). The 5000SF solution's $N_{NB}$ decreased to 0.93 after 2980 min (Fig. 9, orange curve) and held stability for 2540 min divided in five time intervals (Fig. 9, inset plot, orange curve and orange up and down-faced triangles). The hybrid solution (2500SF + 1500NP) $N_{NB}$ decreased to 0.77 in the time interval from $T = 0$ min to $T = 700$ min and 23% of the initial bubbles disappeared (Fig. 9, green curve), this is the same behavior observed in the absence of oil. In the time interval from 700 to 1270 min, the rate of change becomes positive, generation of new bubbles occurs, and the $N_{NB}$ increases to 0.86. The 2500SF + 1500NP solution's $N_{NB}$ decreased to 0.83 after 2980 min and held stability for 1280 min starting from $T = 1620$ min (Fig. 9, inset plot, green curve and green up and down-faced triangles). Doubling the surfactant concentration and adding nanoparticles led to reduction in the stability time for the foams in the presence of the crude oil. As in the absence of oil, in the presence of crude oil, the nanoparticles

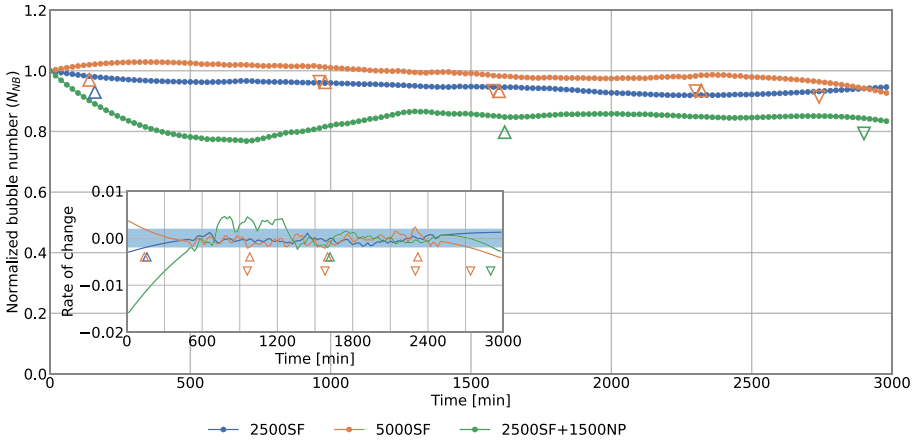


**Fig. 9** The normalized bubble number for experiments conducted with surfactant and nanoparticles-based solutions (2500SF, 5000SF, and 2500SF + 1500NP) in the presence of the crude oil. The data points were smoothed using Savitzky–Golay filter. The inset plot shows the rates of change in the $N_{NB}$. The blue shaded area shows the stability range. The up-faced triangles show the start of the stability, whereas the down-faced triangles show the end of the stability for the different solutions. The foams were in stability in the time intervals: from $T = 160$ min for 2500SF, from $T = 140$ min to 960 min, from 980 to 1580 min, from 1600 to 2300 min, and from 2320 to 2740 min for 5000SF, and from $T = 1620$ min to $T = 2900$ min for 2500SF + 1500NP. The initial bubble number was 131, 34, and 134 for all the solutions in the order presented in the figure. In the presence of the crude oil, doubling the surfactant concentration and adding nanoparticles led to reduction in the stability time

managed to stabilize the foam after the initial decrease in the $N_{NB}$. As the number of lamellae decreased, the concentration of nanoparticles at new lamellae increased, effectively stabilizing the foam.

Foam stability depends on the longevity of individual lamellae (Farajzadeh et al. 2012). Therefore, two locations were examined (Fig. 8, green rectangles) in the FoV for the foam stabilized by the 2500SF solution. The aim was to reveal both the stabilizing and the destabilizing effect of the crude oil on lamellae. Brightfield and red channel images show the location of the crude oil in the pores and lamellae, grains, bubbles, and lamellae (Fig. 10). At location 1, crude oil enters and spreads on most of lamellae, as shown in Fig. 10 b and d where the crude oil can be seen on the lamellae. The two bubbles outlined by the yellow border in Fig. 10.a vanished in the final image (Fig. 10.c). Initially, Ostwald ripening occurred as $CO_2$ diffused from the small bubbles to the largest one. However, the lamellae ruptured, causing the two bubbles to merge with the largest bubble (Fig. 10.c). The bubbles in top right (Fig. 10.a, green circles) were not surrounded by the crude oil and were stable and only moved slightly due to the movement of the largest bubble and crude oil.

At location 2, entering and spreading of crude oil also occurred (Fig. 10, location 2). Initially, oil accumulated at the plateau border, and the oil phase on the lamellae was thin, as shown in Fig. 10.f, where thin crude oil layers can be seen on the lamellae. Throughout time, the oil phase on lamellae thickened and the bubbles were stable throughout the movement of the oil (Fig. 10.h). Based on the observation of the subsequent images and the normalized bubble number, the foam generated with the 2500SF solution was very stable. We did not observe many coarsening events as shown in location 1; instead, the bubbles mostly had the configuration shown in location 2. The crude oil added stability to the $CO_2$ foam generated by the 2500SF and prevented coarsening and coalescence of the bubbles by entering and spreading on lamellae.

The initial bubble number and the stability time for each of the three cases are presented individually in Table 3 to facilitate direct comparison. Overall, the initial bubble number

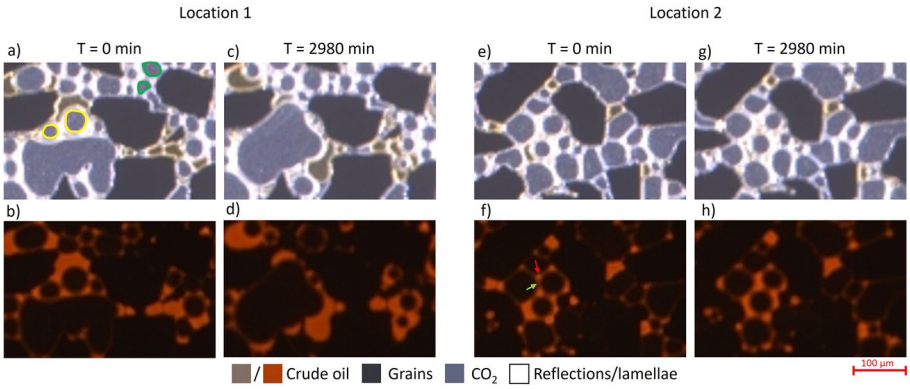


**Fig. 10** Development of static $CO_2$ foam in the presence of the crude oil. Sequential brightfield (upper row) and red (lower row) channel images (total image size 0.41 mm×0.26 mm) at two different locations for the 2500SF solution. The two bubbles marked with yellow circles at location 1 disappear in the last image due to $CO_2$ diffusion and lamella rupture. The crude oil enters lamellae and surrounds the two bubbles, leading to coalescence, while the bubbles marked with green circles were not surrounded by crude and did not disappear. At location 2, oil entering and spreading occurs as well, where the oil accumulates at the plateau border (red arrow), and a thin oil phase spreads on lamellae (green arrow). At $T=2980$ min, the oil phase on lamellae becomes thicker, and the bubbles remain stable throughout the movement of the oil

**Table 3** The initial bubble number and stability time for $CO_2$ foams are provided for the three scenarios: without oil, with immiscible oil, and with miscible oil

| Aqueous solution | No oil | | *n*-Decane | | Crude oil | |
|---|---|---|---|---|---|---|
| | Initial NB [bubble] | Stability time [min] | Initial NB [bubble] | Stability time [min] | Initial NB [bubble] | Stability time [min] |
| 2500SF | 57 | 2720 | 104 | 380 | 131 | 2820 |
| 5000SF | 65 | 1700 | 80 | 440 | 34 | 2540 |
| 2500SF + 1500NP | 76 | 2520 | 97 | - | 134 | 1280 |

increased when an oleic phase, except for the 5000SF in the presence of the crude oil. *n*-Decane reduced the foam stability time for all surfactant solutions, and stability was not reached for the hybrid 2500SF + 1500NP solution. The presence of the crude oil increased stability time for the foams generated by the surfactant solutions, whereas decreased the stability time for the hybrid solution. In the presence of *n*-decane, lamellae rupture was the primary mechanism of foam destabilization. In the presence of the crude oil, however, coarsening became the primary mechanism of foam destabilization as for the absence of oil.

## 4 Conclusion

This work studied the stability of dense-phase $CO_2$ foam generated with different foaming solutions in the presence of miscible (*n*-decane) and immiscible (crude oil) oil in a realistic pore network at 100 bars and 23 °C. In addition, the impact of increasing surfactant concentration and nanoparticles on the foam texture and stability, both in the absence and presence of oil, was investigated. Foam texture became finer with the addition of both *n*-decane and the crude oil, except for the case of 5000SF when the crude oil was present. In the absence of oil, Ostwald ripening (coarsening) was the primary mechanism of foam destabilization. However, when *n*-decane was present, foam destabilization was dominated by lamellae rupture (coalescence). In the presence of the crude oil, Ostwald ripening remained the primary destabilization mechanism based upon entering and spreading of the crude oil within the lamellae. In the absence of oil, foam stability was reduced both when doubling the surfactant concentration and when adding nanoparticles (2500SF: 2720 min; 5000SF: 1700 min; 2500SF + 1500NP: 2520 min). In the presence of *n*-decane, the foam became less stable, and adding nanoparticles led to reduction to half of the initial bubble number (2500SF: 380 min, 5000SF: 440 min, 2500SF + 1500NP: 0 min). When the crude oil was present, $CO_2$ foam maintained stability for longer time compared to the absence of oil for the surfactant-based foams, but stability time decreased when adding nanoparticles (2500SF: 2820 min; 5000SF: 2540 min; 2500SF + 1500NP: 1280 min). The addition of nanoparticles to the surfactant-based foam, and increasing the surfactant concentration, did not increase $CO_2$ foam stability in all cases, except with *n*-decane present where thermodynamically stable micelles/structures were generated.

**Acknowledgements** The authors wish to acknowledge the Research Council of Norway for financial support; project no. 294886 for partial funding PhD candidate for BB; project no. 331841 for partial funding for MF; project no. 331644 for funding PhD candidate HH and partially funding ZPA.

**Funding** This study was funded by Norges Forskningsråd, 294886, Benyamine Benali, 331841, Martin A. Fernø, 331644, Hilde Halsøy, 331644, Zachary Paul Alcorn.

**Data Availability** The raw foam injection micromodel images and python scripts are available from the corresponding author on reasonable request.

## Declarations

**Conflict of interest** The authors declare that they have no known competing financial interests or personal relationships that could have appeared to influence the work reported in this paper.



## References

Alcorn, Z. P., Fredriksen, S. B., Sharma, M., Føyen, T., Wergeland, C., Fernø, M. A., Ersland, G. (2020a). Core-scale sensitivity study of CO2 foam injection strategies for mobility control, enhanced oil recovery, and CO2 storage. *E3S Web Conf., 146*, 02002. Retrieved from https://doi.org/10.1051/e3sconf/202014602002

Alcorn, Z. P., Føyen, T., Gauteplass, J., Benali, B., Soyke, A., & Fernø, M. (2020b). Pore- and Core-Scale Insights of Nanoparticle-Stabilized Foam for CO2-Enhanced Oil Recovery. *Nanomaterials, 10*(10), 1917. Retrieved from https://www.mdpi.com/2079-4991/10/10/1917

Aronson, A.S., Bergeron, V., Fagan, M.E., Radke, C.J.: The influence of disjoining pressure on foam stability and flow in porous media. Colloids Surf. A **83**(2), 109–120 (1994). https://doi.org/10.1016/0927-7757(94)80094-4

Benali, B., Føyen, T.L., Alcorn, Z.P., Haugen, M., Gauteplass, J., Kovscek, A.R., Fernø, M.A.: Pore-scale bubble population dynamics of CO2-foam at reservoir pressure. Int. J. Greenhouse Gas Control **114**, 103607 (2022). https://doi.org/10.1016/j.ijggc.2022.103607

Benali, B., Sæle, A., Liu, N., Fernø, M.A., Alcorn, Z.P.: Pore-level Ostwald ripening of CO2 foams at reservoir pressure. Transp. Porous Media **150**(2), 427–445 (2023)

Benali, B. (2019). *Quantitative Pore-Scale Analysis of CO2 Foam for CCUS.* The University of Bergen,

Bergeron, V., Fagan, M.E., Radke, C.J.: Generalized entering coefficients: a criterion for foam stability against oil in porous media. Langmuir **9**(7), 1704–1713 (1993). https://doi.org/10.1021/la00031a017

Buchgraber, M., Al-Dossary, M., Ross, C.M., Kovscek, A.R.: Creation of a dual-porosity micromodel for pore-level visualization of multiphase flow. J. Petrol. Sci. Eng. **86–87**, 27–38 (2012). https://doi.org/10.1016/j.petrol.2012.03.012

David, A., & Marsden, S. S. (1969). *The rheology of foam.* Paper presented at the Fall Meeting of the Society of Petroleum Engineers of AIME.

Eide, Ø., Føyen, T., Skjelsvik, E., Rognmo, A., & Fernø, M. (2018). In: *Nanoparticle Stabilized Foam in Harsh Conditions for CO2 EOR.* Paper presented at the Abu Dhabi International Petroleum Exhibition & Conference

Eiken, O., Ringrose, P., Hermanrud, C., Nazarian, B., Torp, T.A., Høier, L.: Lessons learned from 14 years of CCS operations: Sleipner, In Salah and Snøhvit. Energy Procedia **4**, 5541–5548 (2011). https://doi.org/10.1016/j.egypro.2011.02.541

Enick, R. M., Olsen, D., Ammer, J., & Schuller, W. (2012). *Mobility and Conformance Control for CO2 EOR via Thickeners, Foams, and Gels - A Literature Review of 40 Years of Research and Pilot Tests.* Paper presented at the SPE Improved Oil Recovery Symposium.

Farajzadeh, R., Andrianov, A., Krastev, R., Hirasaki, G.J., Rossen, W.R.: Foam–oil interaction in porous media: implications for foam assisted enhanced oil recovery. Adv. Coll. Interface. Sci. **183–184**, 1–13 (2012). https://doi.org/10.1016/j.cis.2012.07.002

Føyen, T., Brattekås, B., Fernø, M.A., Barrabino, A., Holt, T.: Increased CO2 storage capacity using CO2-foam. Int. J. Greenhouse Gas Control **96**, 103016 (2020). https://doi.org/10.1016/j.ijggc.2020.103016

Garrett, P.R.: Preliminary considerations concerning the stability of a liquid heterogeneity in a plane-parallel liquid film. J. Colloid Interface Sci. **76**(2), 587–590 (1980). https://doi.org/10.1016/0021-9797(80)90400-2

Gizzatov, A., Pierobon, S., AlYousef, Z., Jian, G., Fan, X., Abedini, A., Abdel-Fattah, A.I.: High-temperature high-pressure microfluidic system for rapid screening of supercritical CO2 foaming agents. Sci. Rep. **11**(1), 3360 (2021). https://doi.org/10.1038/s41598-021-82839-4

Gostick, J.T., Khan, Z.A., Tranter, T.G., Kok, M.D., Agnaou, M., Sadeghi, M., Jervis, R.: PoreSpy: a python toolkit for quantitative analysis of porous media images. J. Open Source Softw. **4**(37), 1296 (2019)

Greenwood, G.: The growth of dispersed precipitates in solutions. Acta Metall. **4**(3), 243–248 (1956)

Hannis, S., Lu, J., Chadwick, A., Hovorka, S., Kirk, K., Romanak, K., Pearce, J.: CO2 storage in depleted or depleting oil and gas Fields: what can we learn from existing projects? Energy Procedia **114**, 5680–5690 (2017). https://doi.org/10.1016/j.egypro.2017.03.1707

Hanssen, J. E., Holt, T., & Surguchev, L. M. (1994). *Foam Processes: An Assessment of Their Potential in North Sea Reservoirs Based on a Critical Evaluation of Current Field Experience.* Paper presented at the SPE/DOE Improved Oil Recovery Symposium.

Huang, Z., Su, M., Yang, Q., Li, Z., Chen, S., Li, Y., Song, Y.: A general patterning approach by manipulating the evolution of two-dimensional liquid foams. Nat. Commun. **8**(1), 14110 (2017). https://doi.org/10.1038/ncomms14110

Jones, S.A., Getrouw, N., Vincent-Bonnieu, S.: Foam flow in a model porous medium: I. The effect of foam coarsening. Soft Matter **14**(18), 3490–3496 (2018). https://doi.org/10.1039/C7SM01903C

Kovscek, A. R., & Radke, C. J. (1993), *Fundamentals of foam transport in porous media*

Lake, L., Johns, R. T., Rossen, W. R., & Pope, G. A. *Fundamentals of Enhanced Oil Recovery*: Society of Petroleum Engineers.

Langevin, D.: Coalescence in foams and emulsions: similarities and differences. Curr. Opin. Colloid Interface Sci. **44**, 23–31 (2019). https://doi.org/10.1016/j.cocis.2019.09.001

Lee, H., Calvin, K., Dasgupta, D., Krinmer, G., Mukherji, A., Thorne, P., Barret, K. (2023). Synthesis report of the IPCC Sixth Assessment Report (AR6), Longer report. IPCC

Eric W. Lemmon, Ian H. Bell, Marcia L. Huber, & Mark O. McLinden. Thermophysical properties of fluid systems. *NIST Chemistry WebBook, NIST Standard Reference Database Number 69, Eds. P.J. Linstrom and W.G. Mallard, National Institute of Standards and Technology, Gaithersburg MD, 20899,* https://doi.org/10.18434/T4D303*, (retrieved February 15, 2023).* https://doi.org/10.18434/T4D303

Lifshitz, I.M., Slyozov, V.V.: The kinetics of precipitation from supersaturated solid solutions. J. Phys. Chem. Solids **19**(1–2), 35–50 (1961)

Liu, N., Haugen, M., Benali, B., Landa-Marbán, D., Fernø, M.A.: Pore-scale kinetics of calcium dissolution and secondary precipitation during geological carbon storage. Chem. Geol. **641**, 121782 (2023). https://doi.org/10.1016/j.chemgeo.2023.121782

Marchalot, J., Lambert, J., Cantat, I., Tabeling, P., Jullien, M.-C.: 2D foam coarsening in a microfluidic system. EPL (europhysics Letters) **83**(6), 64006 (2008)

Metz, B., Davidson, O., De Coninck, H., Loos, M., Meyer, L.: IPCC special report on carbon dioxide capture and storage. Cambridge University Press, Cambridge (2005)

Mo, D., Yu, J., Liu, N., & Lee, R. (2012). *Study of the Effect of Different Factors on Nanoparticle-Stablized CO2 Foam for Mobility Control.* In: Paper presented at the SPE Annual Technical Conference and Exhibition

Pereponov, D., Tarkhov, M., Dorhjie, D. B., Rykov, A., Filippov, I., Zenova, E., Shilov, E. (2023). Microfluidic Studies on Minimum Miscibility Pressure for n-Decane and CO2. *Energies, 16*(13), 4994. Retrieved from https://www.mdpi.com/1996-1073/16/13/4994

Raterman, K. T. (1989). In: *An Investigation of Oil Destabilization of Nitrogen Foams in Porous Media.* Paper presented at the SPE Annual Technical Conference and Exhibition.

Rognmo, A.U., Fredriksen, S.B., Alcorn, Z.P., Sharma, M., Føyen, T., Eide, Ø., Fernø, M.: Pore-to-core EOR upscaling for CO2 foam for CCUS. SPE J. **24**(06), 2793–2803 (2019). https://doi.org/10.2118/190869-pa

Rossen W (1996) Foams in Enhanced Oil Recovery. In: Prud'homme RK, Khan SA (eds) Foams Theory, Measurement, and Applications. New York: Marcel Dekker Inc, pp 413–464

Roy Choudhury, A.K.: 15 - Process control in finishing of textiles. In: Majumdar, A., Das, A., Alagirusamy, R., Kothari, V.K. (eds.) Process control in textile manufacturing, pp. 363–427. Woodhead Publishing (2013)

Sæle, A., Graue, A., Alcorn, Z.: Unsteady-state CO2 foam injection for increasing enhanced oil recovery and carbon storage potential. ADV. IN GEO-ENERGY RES. **6**, 472–481 (2022). https://doi.org/10.46690/ager.2022.06.04

Saint-Jalmes, A.: Physical chemistry in foam drainage and coarsening. Soft Matter **2**(10), 836–849 (2006)

Sarikhani, K., Jeddi, K., Thompson, R.B., Park, C.B., Chen, P.: Adsorption of surface-modified silica nanoparticles to the interface of melt poly(lactic acid) and supercritical carbon dioxide. Langmuir **31**(20), 5571–5579 (2015). https://doi.org/10.1021/acs.langmuir.5b00306

Schramm, L.L., Novosad, J.J.: Micro-visualization of foam interactions with a crude oil. Colloids Surf. **46**(1), 21–43 (1990)

Shan, D., Rossen, W.R.: Optimal Injection Strategies for Foam IOR. SPE J. **9**(02), 132–150 (2004). https://doi.org/10.2118/88811-pa

Sheng, J.J.: Chapter 11 - foams and their applications in enhancing oil recovery. In: Sheng, J.J. (ed.) Enhanced Oil Recovery Field Case Studies, pp. 251–280. Gulf Professional Publishing, Boston (2013)

Singh, R., & Mohanty, K. K. (2014). *Synergistic stabilization of foams by a mixture of nanoparticles and surfactants. In:* Paper presented at the SPE improved oil recovery symposium.

Soyke, A., Benali, B., Føyen, T., Alcorn, Z.P.: Hybrid nanoparticle-surfactant stabilized foams for CO2 mobility control at elevated salinities. Euro. Assoc. Geosci. Eng. **2021**(1), 1–14 (2021). https://doi.org/10.3997/2214-4609.202133110

Steinsbø, M., Brattekås, B., Fernø, M., Ersland, G., & Graue, A. (2014). *Supercritical CO2 injection for enhanced oil recovery in fractured chalk. In:* Paper presented at the International Symposium of the Society of Core Analysts

Taber, J.J., Martin, F.D., Seright, R.S.: EOR screening criteria revisited— part 1: introduction to screening criteria and enhanced recovery field projects. SPE Reserv. Eng. **12**(03), 189–198 (1997). https://doi.org/10.2118/35385-pa

Talebian, S.H., Masoudi, R., Tan, I.M., Zitha, P.L.J.: Foam assisted CO2-EOR: a review of concept, challenges, and future prospects. J. Petrol. Sci. Eng. **120**, 202–215 (2014). https://doi.org/10.1016/j.petrol.2014.05.013

Voorhees, P.W.: The theory of Ostwald ripening. J. Stat. Phys. **38**(1), 231–252 (1985)

Voorhees, P.W.: Ostwald ripening of two-phase mixtures. Annu. Rev. Mater. Sci. **22**(1), 197–215 (1992)

Wang, H., Li, J., Wang, Z., Wang, D., Zhan, H.: Experimental investigation of the mechanism of foaming agent concentration affecting foam stability. J. Surfactants Deterg. **20**(6), 1443–1451 (2017). https://doi.org/10.1007/s11743-017-2004-2

Xu, K., Bonnecaze, R., Balhoff, M.: Egalitarianism among bubbles in porous media: an ostwald ripening derived anticoarsening phenomenon. Phys. Rev. Lett. **119**(26), 264502 (2017)

Xu, K., Mehmani, Y., Shang, L., Xiong, Q.: Gravity-induced bubble ripening in porous media and its impact on capillary trapping stability. Geophys. Res. Lett. **46**(23), 13804–13813 (2019). https://doi.org/10.1029/2019GL085175

Yu, W., Kanj, M.Y.: Review of foam stability in porous media: the effect of coarsening. J. Petrol. Sci. Eng. **208**, 109698 (2022). https://doi.org/10.1016/j.petrol.2021.109698

Yu, W., Zhou, X., Kanj, M.Y.: Microfluidic investigation of foam coarsening dynamics in porous media at high-pressure and high-temperature conditions. Langmuir **38**(9), 2895–2905 (2022). https://doi.org/10.1021/acs.langmuir.1c03301